Ceramics International 48 (2022) 14127–14140

Contents lists available at ScienceDirect

Ceramics International

journal homepage: www.elsevier.com/locate/ceramint

Microstructure and properties of metal parts remanufactured by laser cladding TiC and TiB_2 reinforced Fe-based coatings

Liaoyuan Chen [a], Tianbiao Yu [a,*], Chuang Guan [a], Yu Zhao [b]

[a] School of Mechanical Engineering and Automation, Northeastern University, Shenyang, China
[b] School of Mechanical and Aerospace Engineering, Jilin University, Changchun, Jilin, China

ARTICLE INFO

Keywords:
Surface remanufacturing
In situ TiC–TiB_2
Microstructure and phase evolution
Mechanical properties

ABSTRACT

Laser cladding process, an efficient surface remanufacturing method, has become a research hotspot in recent years. Herein, *in situ* titanium carbide (TiC) and titanium diboride (TiB_2) reinforced composite coatings were fabricated on the surface of damaged carbon steel to improve the hardness and wear resistance of remanufactured parts. Effects of addition of $5B_4C$ and 15Ti (in wt.%) powder on morphology, phase composition, microstructure, and mechanical properties of specimens were comprehensively investigated. Results revealed that milled groove could be effectively filled with composite coating, which formed good metallurgical bonding with the substrate. Furthermore, sequentially precipitated *in situ* synthesized phases including TiC, TiB_2, Cr_3C_2, Fe_2B, and Fe_3C in composite coating could continuously increase nucleation sites and further refine grains. Moreover, uniformly distributed reinforcements effectively weakened the directivity of heat flow during solidification process and promoted columnar to equiaxed transition. Mechanical properties illustrate that micro-hardness of composite coating with 961.94 $HV_{0.3}$ is 4.14 and 5.04 times, and corresponding volume loss is 7.8 and 2.8 less than those of 316 L coating and standard 45 steel, respectively. This study indicates that *in situ* formed ceramics reinforced composite coating can act as an ideal candidate for remanufacturing damaged parts, and further improve their wear resistance.

1. Introduction

Recently, the global industrialization boom has put forward higher requirements for the rotation speed, carrying capacity, and excellent fatigue life of metal parts in mechanical processing, transportation, and aerospace, other mechanical equipment industries. Therefore, the remanufacturing of damaged metal parts is of great significance for prolonging the service life, improving the resources utilization, promoting industrial transformation, and coping with various challenges of sustainable development [1,2]. Laser cladding is one of the advanced additive manufacturing (AM) processes, which has been proven to be effective in manufacturing composite coatings with excellent mechanical properties on the surface of new or damaged parts [3,4]. Compared to the other remanufacturing technologies (i.e., arc welding, cold spray, and plasma spray), coaxial laser cladding has shown extraordinary advantages, such as wide material applicability, flexible scanning strategies design and rapid response to market demand, in remanufacturing and surface modification of metal parts [5–7]. Furthermore, the damage of rare materials can be reduced or even prevented during the remanufacturing process.

Iron (Fe) and Fe-based alloys are the most widely used metal materials in industrial applications due to their mature production process, good machinability, and cost-effectiveness. Many researchers have carried out in-depth studies on the remanufacturing of surface defects of Fe-based parts. For instance, Graf et al. [7] filled U and V-shaped milled grooves with stainless steel and Ti–6Al–4V powder by laser metal deposition technique. The results showed that the defect-free repair regions could be developed as long as the groove width was wide enough for good powder jet accessibility. Li et al. [8] investigated the effect of designed scanning strategies and groove shape on the bonding properties of the deposited coating. They reported that the macro defect in the repaired region could be reduced under the cross-scanning strategy. Zhu et al. [9] reconstructed a three-dimensional (3D) model of the broken tooth via reverse engineering technology, and then completed the

---

[*] Corresponding author. School of Mechanical Engineering and Automation, Northeastern University, NO. 3-11, Wen hua Road, He ping District, Shenyang, 110819, PR China.

E-mail addresses: chen1910113@163.com (L. Chen), tianbiaoyudyx@gmail.com (T. Yu), guanchuang10193@163.com (C. Guan), zhaoyuneu@gmail.com (Y. Zhao).

https://doi.org/10.1016/j.ceramint.2022.01.299
Received 31 July 2021; Received in revised form 11 January 2022; Accepted 27 January 2022

remanufacturing of damaged 45 steel gear by laser cladding. Sun et al. [10] explored the fatigue behavior of repaired zones fabricated on ultra-high-strength AISI 4340 steel and pointed out that the local heat treatment could reduce the residual stress and heat affected zone (HAZ). Thus, the stated literature studies indicate that laser cladding is an effective method to realize the remanufacturing of damaged parts. To the best of our knowledge, previous studies always focused on the bonding performance between the remanufactured zone and the substrate; nonetheless, low hardness and poor wear resistance of remanufactured zones have rarely been investigated.

To date, the strengthening mechanism and fabrication process of metal matrix composite (MMC) coatings with high hardness, excellent corrosion resistance, and good wear resistance have been thoroughly and comprehensively investigated by many scholars [11–14]. These MMC coatings are usually composed of matrix phases (i.e., Fe, Ni, Co alloys) and reinforcement phases (i.e., carbides, borides, and intermetallics) [15,16]. Among these MMC materials, ceramic reinforced iron (Fe)-based or nickel (Ni)-based coatings have received continuous interest because of their good interfacial bonding performance, designable composition, and low fabrication cost. Wang et al. [17] studied the effect of TiC particle size on the microstructure and mechanical properties of Ti-based composites. The tensile strength and elongation of Ti-based composites could be improved by adding ultrafine TiC particles (<10 μm). Besides, some microcracks were also observed in large and unmelted TiC particles. Briefly, the pores and cracks often appeared in MMC coatings prepared by directly adding coarse ceramics particles, which seriously limited the practical application of ceramic reinforced MMCs in remanufacturing process [11,15]. In order to solve the above mentioned problems, progressively more attention has been paid to the advantages of *in situ* formed ceramic particles in MMC coatings by AM, which offers better thermal stability and interfacial compatibility to transfer stress [18–20]. For instance, Wang et al. [21] produced *in situ* TiC particles reinforced Fe-based composite coatings on the surface of AISI 1020 steel by multi-pass overlapping gas tungsten arc welding melting process and found that coarse dendrite shape TiC appeared in the overlap zone. Cui et al. [22] found that the TiC particle size increased from 5 to 10 μm with the increase in the Ti + C content from 14 to 20 wt%. Coarsening of TiC particles would lead to the embrittlement of the MMCs, and reduce the hardness and wear resistance.

Although the mechanism and advantage of *in situ* ceramic reinforced Fe- or Ni-based coatings have been revealed, the practical application of *in situ* formed ceramics reinforced coatings during the surface remanufacturing of damaged parts has rarely been investigated to date. Notably, TiB_2 and TiC ceramics show excellent properties, such as high melting point, high hardness and modulus, and high-temperature stability, and have been proven to be effective candidates for improving the mechanical performance of coatings [23–26]. In this study, the surface remanufacturing of damaged medium carbon steel was realized by the *in situ* formed ultrafine TiB_2 and TiC reinforced Fe-based coating. The macro morphology, phase constitution, microstructure, micro-hardness and wear resistance of the remanufactured zone were investigated and discussed in detail. The main objective of this study was to apply laser-clad ceramics reinforced composite coating to the surface remanufacturing of damaged parts and further improve their industrial application.

2. Remanufacturing strategy

2.1. Material preparation

Commercial AISI316L (316 L) stainless steel powder with the size of 100–200 μm, pure B_4C powder with the size of 60–120 μm, and pure Ti powder with the size of 2–3 μm were used in this study. The remanufactured part was the most commonly used medium carbon steel plate with the size of $50 \times 50 \times 10$ mm^3. The nominal compositions of 316 L and standard 45 steel are listed in Table 1. The reaction ($3Ti + B_4C \rightarrow 2TiB_2 + TiC$) investigated in this study for TiC and TiB_2 phases was expected to occur during laser cladding process, thus the mass percentages of Ti and B_4C were selected to be as 15 and 5 wt%, respectively, when the oxidation of B_4C powder was considered. The laser-clad powder compositions (in wt.%) for designed specimens are as follows, specimen 1#: 316 L powder without adding B_4C and Ti powders and specimen 2#: 316 L-5B_4C–15Ti composite powders. The density values of TiB_2, TiC, and α-Fe are about 4.52, 4.99, and 7.8 g cm^{-3}, respectively [26], therefore, the designed volume fraction of the TiC–TiB_2 phases in specimen 2# is 29.47%. Fig. 1 shows the mixing process of 316 L-5B_4C–15Ti composite powders. Briefly, following steps are involved in the process: (1) Each powder was weighed by digital electronic balance (accuracy 0.01 mg). (2) Composite powders were mixed by ball milling at 450 rpm for 2 h, using alumina with ball-to-powder weight ratio of 2:1. (3) Then, sieve with 80 mesh was used to remove dirt from the composite powders. (4) Before the experiment, the powders were dried in a drying oven at 80 °C for 2 h to remove moisture.

2.2. Laser cladding process

The laser cladding system used in the experiment consists of a KUKA robot, a coaxial powder feeding nozzle, a controller, a laser generator, a water cooler, and an electric control cabinet. The flexible KUKA robot could meet the flexible scanning strategies for different complex parts. A coaxial powder feeding nozzle (RC52) is installed at the end effector of the KUKA robot (R16-2). The deposition energy is provided using a fiber laser generator (wavelength 1020 nm, maximum power 500 W) with a continuous wave. More details of the laser cladding system can be found in our previous study [27]. The distance from the deposition plate to the bottom of the powder feeding nozzle is 15 mm, and the laser beam on the deposition plane is about φ1.0 mm. Argon (purity, 99.99%) with a flow rate of around 20 and 8 L min^{-1} was used as the shielding gas and powder deliver gas, respectively. The optimized parameters for 316 L are obtained from the previous study [28] and listed in Table 2.

Fig. 2 shows the schematic illustration of the remanufacturing process. The designed scanning strategy is shown in Fig. 2(a), which was precisely controlled by using offline programming software (Robot Art). In general, it was initially believed that a larger coating thickness can improve the service life of the coating. However, with the increase of coating thickness, the residual stress in the coating fabricated by AM also increases, which can lead to the spontaneous falling off of the coating from the substrate [29,30]. The groove depth selected in this study was 2.0 mm according to the study by Hutasoit et al. [31], as shown in Fig. 2(b). The distance between the two tracks in each layer and the Z-axis increment was set as 0.4 and 0.5 mm, respectively, based on the results of planar scanning experiments. The single-layer height varies depending on process parameters, substrate shape, and powder properties [32]. Therefore, the filling state of the groove after the

Table 1
Chemical compositions of 316 L powder and standard 45 steel.

Element (wt. %)	C	Cr	Mo	Si	Ni	Mn	Cu	P	Fe
316 L	0.03	18.62	2.53	0.54	12.72	1.35	–	–	Bal.
45steel	0.42–0.50	≤0.2	–	0.17–0.37	≤0.30	0.50–0.80	≤0.25	≤0.035	Bal.

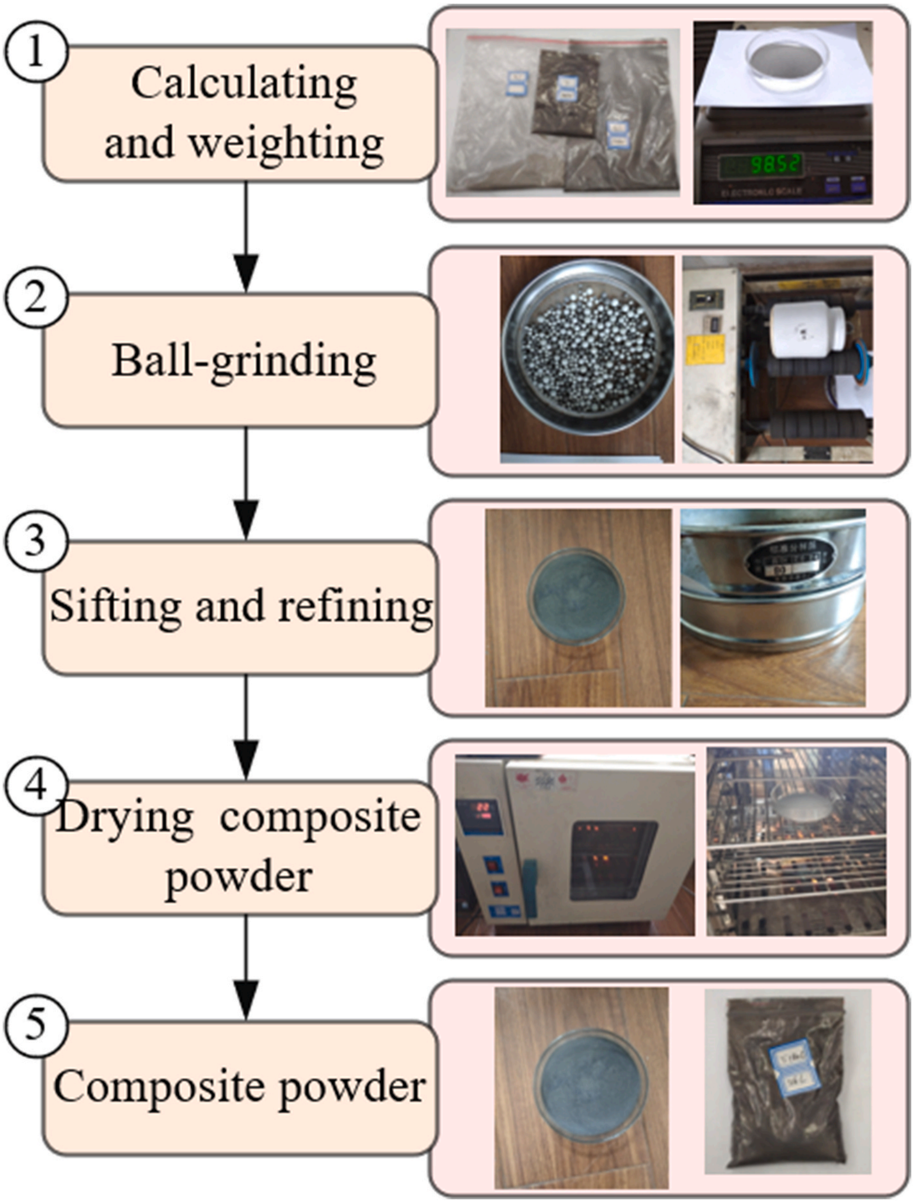

Fig. 1. The preparation process of 316 L-5B_4C–15Ti composite powders.

Table 2
The processing parameters for laser cladding.

Laser	Output power	Beam diameter	Scan speed	Shielding gas	Powder feed rate
YAG laser	350	1.0 mm	5.5 mm/s	Argon	7.72 g/min

deposition of each layer was observed in real-time. The experiment ended immediately when the groove was completely filled with the coatings.

2.3. *Characterization*

After the experiment, the remanufactured parts were allowed to cool to room temperature (20 °C) in the air. To evaluate the microstructure and mechanical properties in the remanufactured zone, the test specimens (20 × 12 × 10 mm^3) were cut from the substrate along the rectangular direction 1 by wire electrical discharge machining, as shown in Fig. 2(a). The height of the remanufactured parts was measured using a three-coordinate measuring machine (HEXAGON, China). The location of the characterization on the remanufactured specimen is shown in Fig. 2(c). For characterizing the microstructure and phase constitution of the remanufactured specimen, the planes A and B were ground with 240, 400, 600, 800, 1000, 1500, and 2000 grit size SiC sandpapers, and polished, respectively. The phase constitution on plane B was investigated by X-ray diffraction (XRD, X-Pertpro, Netherlands) with Cu Kα radiation and an 8°/min scanning rate in the range of $10^\circ \leq \theta \leq 90^\circ$. The size, color, and distribution of phases were revealed on Plane A (electrochemically in 10 wt% oxalic acid solution for 5–20s at 15 V and 1.0 A) by scanning electron microscopy (SEM, Zeiss, Germany) system equipped with an energy dispersive spectrometry (EDS) system. All test specimens were ultrasonically cleaned in distilled water for 2 min to remove dirt. Microstructural characteristics were obtained by optical 3D laser microscopy (OLS 41000, Japan). The micro-hardness of each specimen was measured on Plane B by Vickers diamond indentation (HV-1000, China) with a 0.3 kg load and 15 s dwell time, at a 100 μm equidistant point. The wear performance was investigated on Plane B (Ra <0.02 μm) using a reciprocating sliding tester (MFT-4000, China).

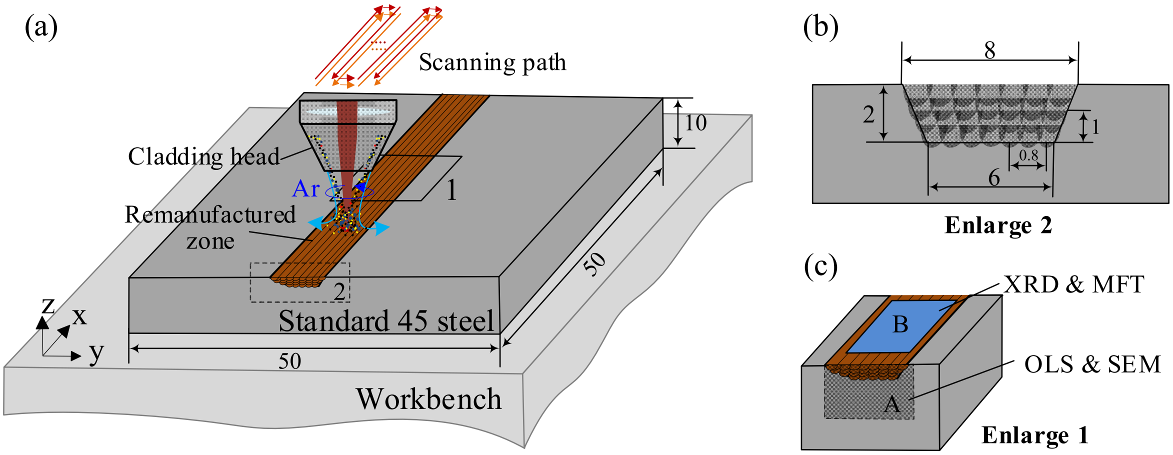

Fig. 2. Schematic illustration of the remanufacturing process: (a) scanning strategy, (b) designed groove, and (c) test specimen.

The material used for the friction pair was alumina with a hardness of 90–98 HRC. Parameters of sliding wear process are listed in Table 3. The 3D morphology of the worn surface was also revealed using OLS4100 microscopy.

3. Results and discussion

3.1. Morphologies

Fig. 3(a1) and (b1) show the morphologies of the remanufactured parts processed using specimen 1# with three layers and specimen 2# with four layers. No obvious surface defects (pores and cracks) were observed at the top of the two specimens. Specimen 1# was white and bright, while specimen 2# was gray and dark. The active element Ti could easily react violently with O_2 and N_2 in the air to generate TiO_2 and TiN particles, respectively, at high temperatures [16,33]. These slags inclusion precipitated from the molten pool to form black particles, which attached to the surface of specimen 2#. Ma et al. [16] also observed a similar phenomenon. This oxidation behavior resulted in the reduction in Ti concentration, and further decrease in the volume fraction of *in situ* ceramic phases. The increase of shielding gas rate could reduce the oxidation of the Ti element. Besides, the active element Ti could combine with impurity elements (i.e., sulfur, phosphorus) to form low melting point alloys, which was found to be beneficial to improve the compactness of specimen 2#. Therefore, the height of specimen 2# is significantly lower than that of specimen 1#, as shown in Fig. 3(a_2) and (b_2). Previous studies [34,35] showed that the surface smoothness could not only reduce the damage of valuable materials, but also indirectly improve the lapping quality between two tracks. Fig. 4 illustrates that the lower standard deviation (STDEV) of specimen 2# indicates a better profile. The key to fabricating parts with high dimensional accuracy by AM is to maintain the dynamic balance between the single-layer height and the Z-axis increment [36,37]. The single-layer deposition height of specimen 2# is 0.65 mm, which is slightly larger than the Z-axis increment (0.5 mm). However, the single-layer height (about 1.0 mm) of specimen 1# was much larger than the Z-axis increment, indicating the occurrence of over deposition. The laser energy presents a Gaussian distribution; therefore, the energy density decreases during the laser cladding [38]. Both over-deposition and under-deposition result in a difference between the signal-pass deposition thickness and the Z-axis increment, and the geometric error increases with the progress of the deposition [39]. The deposition energy is not enough to completely melt the precursor, thus the top surface of specimen 1# exhibits the appearance of irregular wave shape, as shown in Fig. 3(a).

Table 3
Sliding wear process parameters.

Parameters	Values
Friction pair (mm)	φ5 Al_2O_3
Specimens size (mm^3)	15 × 15 × 10
Load (N)	15
Wear time (min)	50
Reciprocating distance (mm)	6
Grinding Speed (mm min^{-1})	220
Temperature (°C)	25 °C

3.2. Phase and thermodynamic analysis

The XRD profiles of different specimens are presented in Fig. 5. The phase compositions of specimen 1# include austenite [Fe–Cr] solid solution for typical AM 316 L part [40]. Compared with the XRD spectrum of specimen 1#, some new diffraction peaks are observed for specimen 2#. These new peaks in the diffraction spectrum at 35.01°, 40.67°, 59.51°, and 74.99° could be well indexed to titanium carbide (JCPDS No.00-006-0614 for TiC). Besides, titanium boride diffraction peaks (28.10°, 34.64°, 44.96°, 79.18°, JCPDS No.01-085-2083 for TiB_2) are also observed for specimen 2#. These results indicate the successful *in situ* synthesis of TiC and TiB_2 in the composite coating. Moreover, the Fe_3C (JCPDS No. 96-230-0071), Cr_3C_2 (JCPDS No. 03-065-0897), [Fe–Ni] solid solution (JCPDS No. 00-003-1109), and Fe_2B (JCPDS No.01-075-1062) phases were also detected for specimen 2#.

To identify each phase distinctly, SEM and EDS analysis were conducted, and the corresponding results are presented in Fig. 6 and Table 4. Fig. 6 exhibits that specimen 2# is mainly composed of complex phases including particle-shaped (A), strip-shaped (B), fine granular (C), precipitated lump (D), matrix (E), and a small amount of rod-shaped (F). Table 4 lists that particle-shaped structures (A1) and polygonal structures (A2) are mainly composed of Ti and C atoms with an atomic ratio of 1:1, and these can be identified as TiC phases combined with the XRD results. The strip-shaped phase (B) is enriched with Ti and B according to EDS mapping result, as shown in Fig. 7, and it is equipped with the geometric characteristics of TiB_2 in AM Fe-based coating [41,42]. Therefore, this strip-shaped phase can be proved as TiB_2. In addition, some fine granular phases (C) are found in precipitated lump (D). As listed in Table 4, these phases contain C and Cr elements, and can be ascribed to Cr_2C_3 by the XRD and EDS results [43]. According to EDS result of point (D), the atomic ratio between Fe and B is near 2:1. It can be regarded as Fe_2B, which is in accordance with previous study [44]. Moreover, EDS results also can reveal that the phases E and F can be identified as the [Fe–Ni] solid solution and Fe_3C, respectively. EDS mapping scanning results of each element in the enlarged region of Fig. 6(b) are presented in Fig. 7. The [Ti] element is evenly distributed in

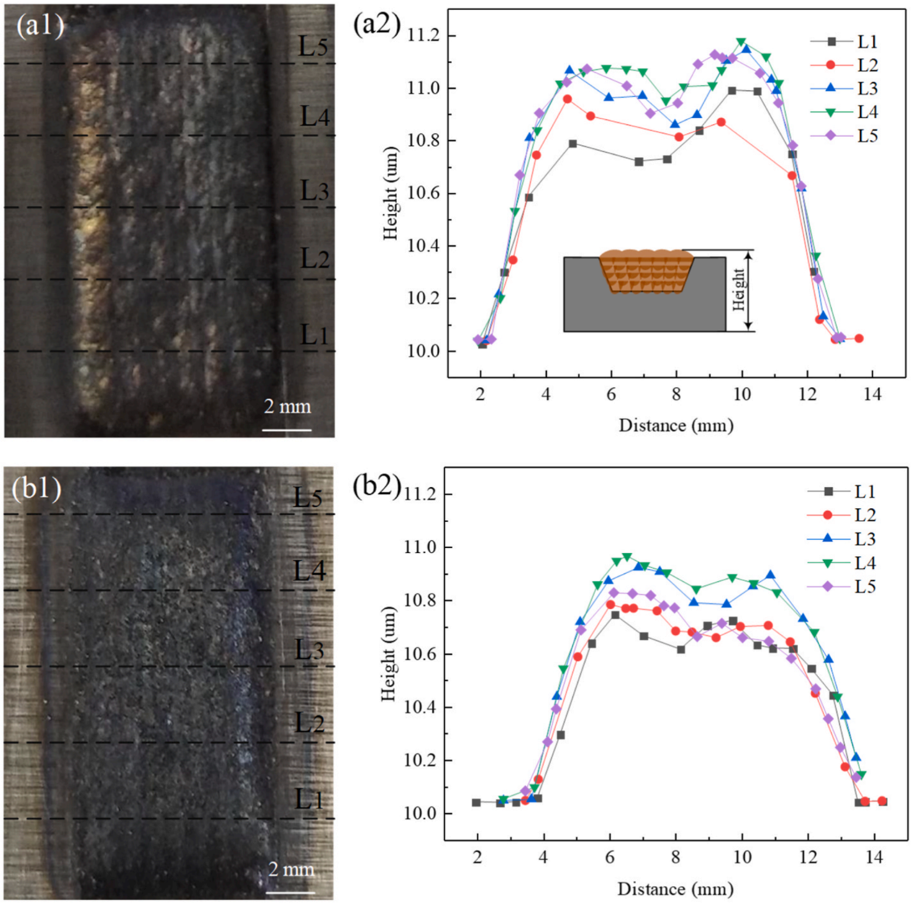

Fig. 3. Surface topographies and height measurement results of (a) specimen 1# and (b) specimen 2#.

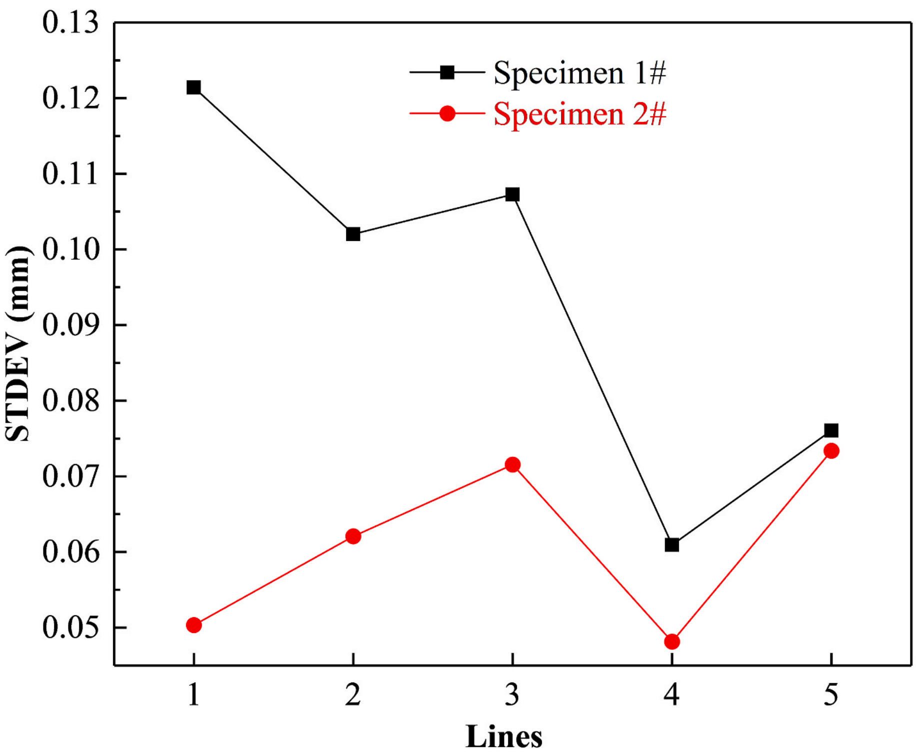

Fig. 4. The STDEV results on different lines.

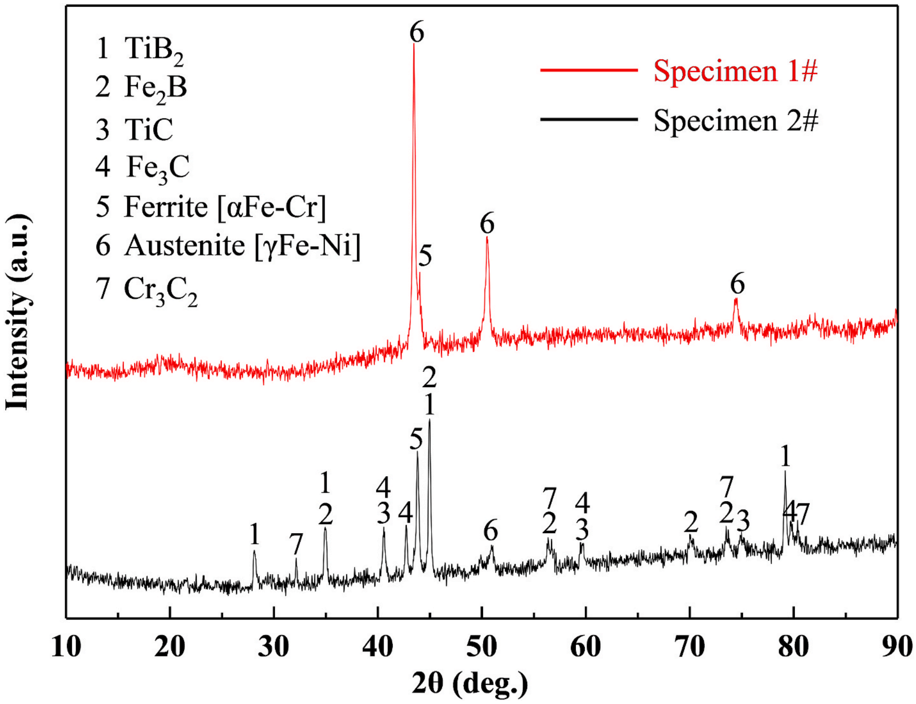

Fig. 5. XRD spectra of specimen 1# and specimen 2#.

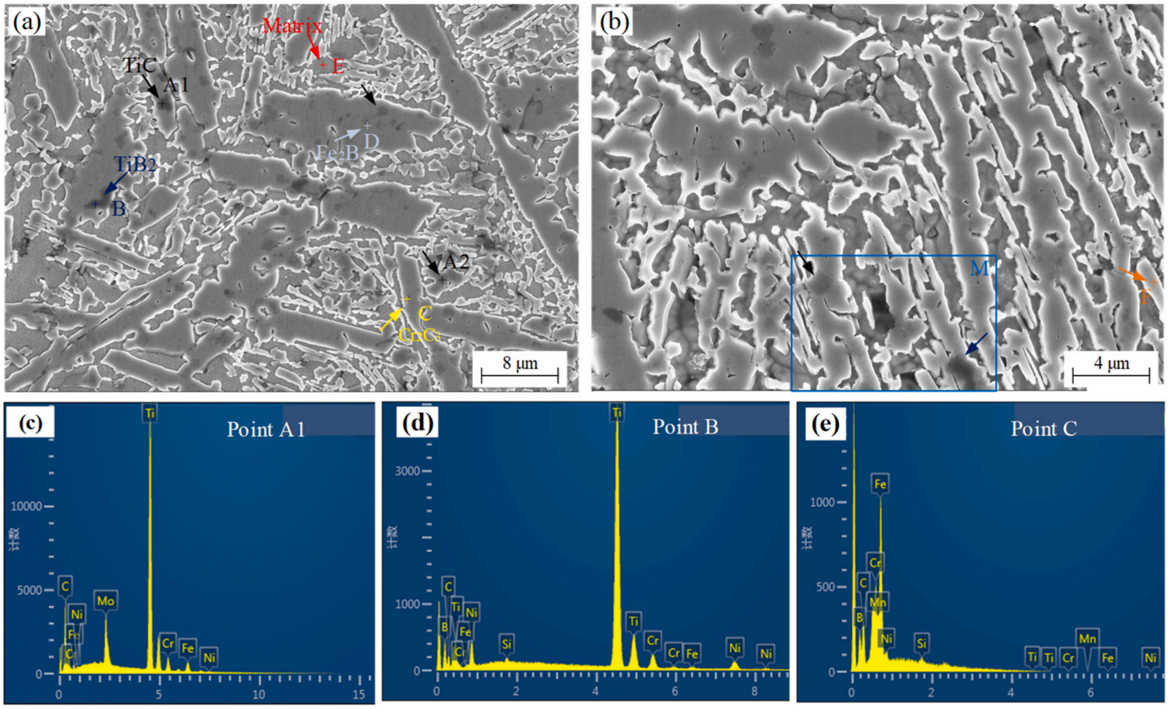

Fig. 6. SEM micrographs of specimen 2# at (a) 5kx, (b) 10kx, and corresponding EDS results of (c) Point A1, (d) Point B, and (e) Point C.

specimen 2#, and its distribution position is consistent with those of [C], [B], and [Mo] elements. This indicates that *in situ* formed TiC particles are uniformly distributed. Moreover, [Mo] elements can inhibit the growth of TiC and TiB_2, which is in good agreement with the research by He et al. [45].

For the deep revelation of the formation mechanism of reinforcement phases in specimen 2#, the Gibbs free energy (ΔG_T^{Θ}) of potential reactions $1^{\#}$–$6^{\#}$ were calculated combined with the XRD results.

$$Ti + 2B \rightarrow TiB_2 \quad 1^{\#}$$

$$Ti + C \rightarrow TiC \quad 2^{\#}$$

$$Ti + B \rightarrow TiB \quad 3^{\#}$$

$$3Cr + 2C \rightarrow Cr_3C_2 \quad 4^{\#}$$

Table 4
EDS results of different phases marked in Fig. 6 (at. %).

Analyzed points	Ti	C	B	Cr	Mo	Si	Ni	Mn	Fe
A1	42.14	47.94	–	3.20	3.24	–	0.34	–	3.14
A2	44.10	42.33	–	4.24	3.51	–	0.48	0.29	5.05
B	28.27	6.1	58.76	3.62	–	0.21	0.66	–	2.38
C	0.46	50.93	4.35	36.10	–	0.48	0.58	–	7.10
D	0.30	9.22	20.55	23.67	1.02	0.06	1.25	1.17	42.76
E	0.78	0.50	–	5.70	0.85	3.88	16.28	1.75	70.26
F	1.03	28.26	–	4.99	0.79	4.20	12.73	1.15	46.85

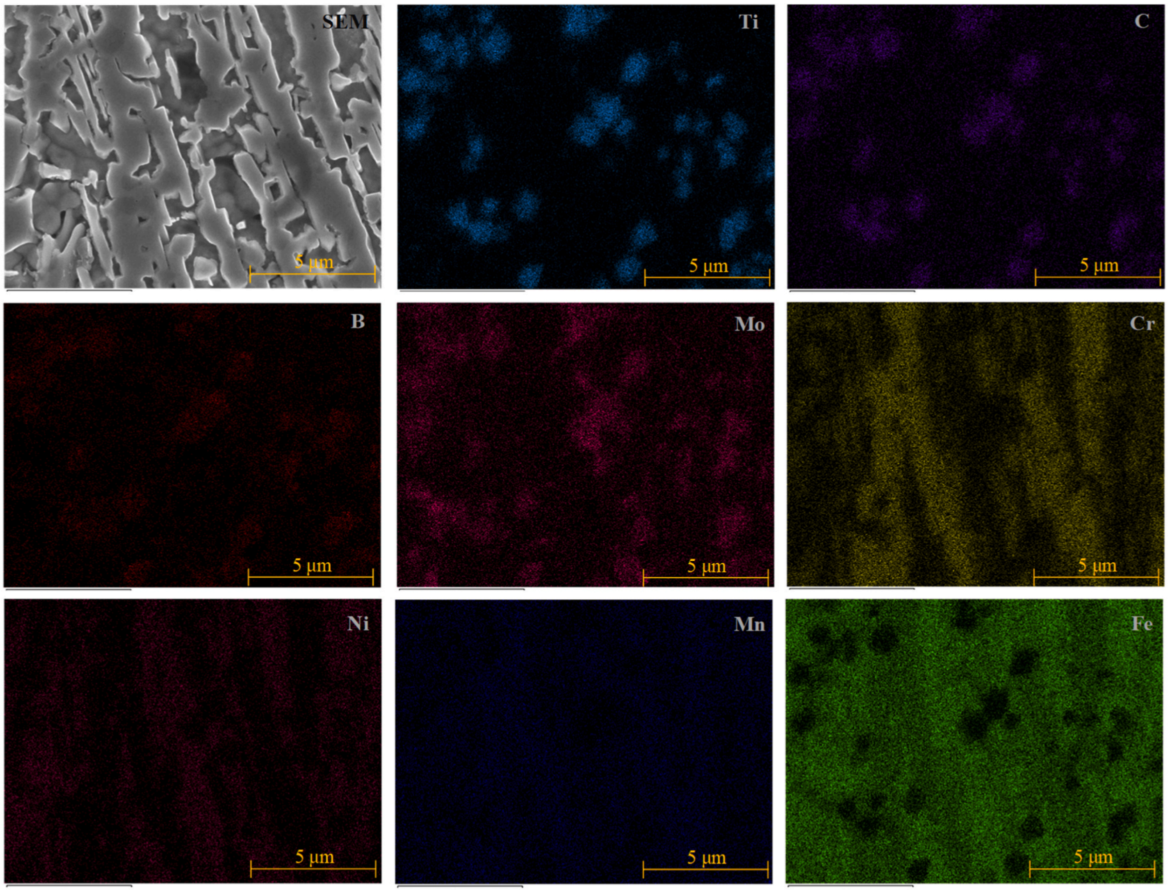

Fig. 7. The EDS scan and elemental maps of Ti, C, B, Mo, Cr, Ni, Mn, and Fe elements from specimen 2#.

$2Fe + B \rightarrow Fe_2B$ $5^{\#}$

$3\mathbf{Fe} + \mathbf{C} \rightarrow \mathbf{Fe_3C}$ $6^{\#}$

The $\Delta G_{\mathbf{T}}^{\Theta}$ can be expressed in terms of the following equations:

$$\Delta G_{\mathbf{T}}^{\Theta} = \sum G_{\mathbf{product}}^{\Theta}(T) - \sum G_{\mathbf{reactant}}^{\Theta}(T) \tag{1}$$

where the first and second terms on the right side of Eq. (1) represent the total $\Delta G_{\mathbf{T}}^{\Theta}$ of the product or reactant, respectively. The $G_i^{\Theta}(T)$ of the *i*th reactant or product can be defined as Eq. (2).

$$G_i^{\Theta}(T) = H_i^{\Theta}(\mathbf{T}) - \mathbf{T} \cdot S_i^{\Theta}(\mathbf{T}) \tag{2}$$

where $H_i^{\Theta}(T)$ and $S_i^{\Theta}(\mathbf{T})$ are the enthalpy and standard entropy, respectively. The phase change $(H_i^{\Theta}(T))$ is considered in this study, which is expressed by Eq. (3) as follows:

$$S_{\mathrm{i}}^{\Theta}(T) = \Delta_{\mathrm{f}} H_i^{0}(298) + \int_{298}^{\mathbf{T}} C_{Pi}(\mathbf{T}) d\mathbf{T} + \Delta H_i^{\Theta}(\mathbf{T}_m) \tag{3}$$

where $\Delta_{\mathrm{f}} H_i^{0}(298)$ is the enthalpy at 298 K and $\Delta \mathbf{H}_i^{\Theta}(\mathbf{T}_m)$ is the latent heat of the substance. The material parameters for thermodynamic calculations are based on the thermodynamic properties of the inorganic materials manual [46]. The Gibbs free energy of each reaction is shown in Fig. 8. $\Delta G_{\mathbf{T}}^{\theta}(\text{reaction}1^{\#} - 5^{\#}) < 0$ indicates that the expected carbide and boride compounds could be spontaneously nucleated and *in situ* formed. Besides, the larger $|\Delta G_{\mathbf{T}}^{\theta}(\text{reaction}1^{\#}\text{and } 2^{\#})|$ shows that *in situ* formed TiC and TiB_2 phases exhibit better stability. To significantly explore the microstructure evolution mechanism of remanufactured specimen 2# in detail, schematic illustration of multiphase evolution during solidification process was obtained, as shown in Fig. 9.

The 316 L-5B_4C–15Ti composite powders were rapidly heated and completely melted with the laser beam to form Fe–Ti–B–C–Cr multi-component liquid phases (MLPs), as shown in Fig. 9(a). This largely contributes to strong convection velocity (>200 mm/s) and high-temperature (>3000 K) [44]. The melting point of TiC is higher than that of TiB_2, and the thermal diffusivity of the [C] element is higher than that of the [B]; therefore, TiC phases first precipitated from the MLPs at

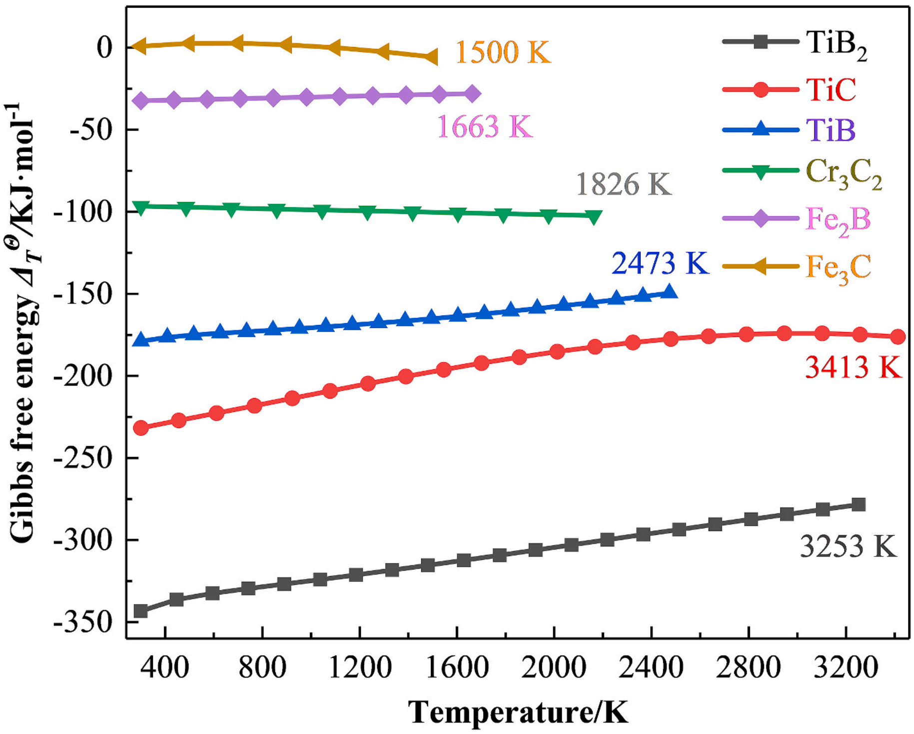

Fig. 8. The calculated Gibbs free energy of possible reactions in specimen 2#.

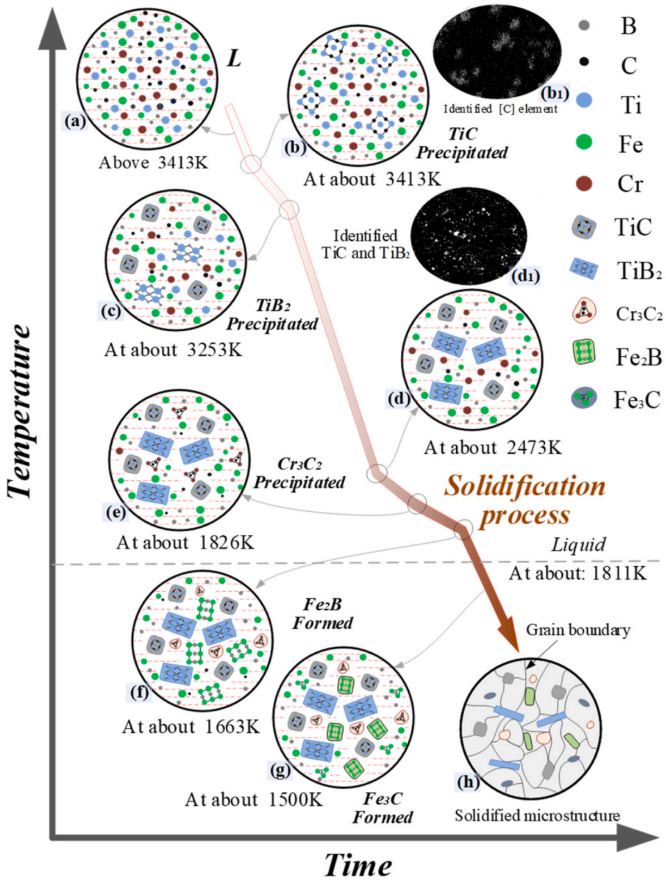

Fig. 9. The schematic illustration of multiphase evolution in specimen 2# during solidification process.

about 3413 K, as shown in Fig. 9(b). In view of the cubic crystal system and crystallographic orientation (111) of the TiC, solidified TiC phases are mostly round shape with small size or relatively regular rectangle shape with large size. This is similar to the phenomenon found by Moghaddam et al. [33]. From $|\Delta G_T^\theta|$, the order of reactions below 3253 K is $1^\# > 3^\# > 4^\# > 5^\# > 6^\#$. When the temperature decreased to the melting point (3253 K) of TiB$_2$, [Ti] atoms exhibited a larger tendency to react with [B] atoms rather than with [C] atoms to form TiB$_2$ phases because of the lowest $|\Delta G_T^\theta[reaction1^\#]|$, as shown in Fig. 9(c). Fig. 6 demonstrates that the solidified TiB$_2$ exhibits hexagonal or rhombohedral structure due to its hexagonal crystal system and (0001) orientation. No diffraction peaks of TiB are found in Fig. 5, which illustrates that the TiB phase was not formed in the MLPs at about 2473 K. On the one hand, the oxidation of B$_4$C resulted in further increase in the atomic ratio between [Ti] and [B]. When the precipitation of TiB occurs during the solidification process, the rich-[B] element in the MLPs stimulates the reaction (TiB + B→TiB$_2$) and promotes the transformation of TiB to TiB$_2$. On the other hand, the TiB$_2$ phase enjoys the most robust crystal structure stability among all the compounds formed with boron and titanium. Furthermore, the volume fraction of the identified TiC–TiB$_2$ phases is 4.35%, as shown in Fig. 9(d1), which is far less than the designed value (29.47 vol%). The oxidation of precursor materials and harsh *in situ* reaction conditions restricted the fabrication of high-volume fraction ceramic materials by AM [47]. As shown in 9, the metal liquid rapidly solidified into [Fe–Ni] solid solution at about 1811 K after precipitation of Cr$_2$Cr$_3$ at about 1826 K. Therefore, Cr$_2$Cr$_3$ particles are fine round and dispersed in the matrix, as shown in Fig. 6. With the further decrease of temperature, a large amount of Fe$_2$B phase was *in situ* synthesized at about 1663 K due to the remaining rich-[B] and [Fe] elements in the matrix. The formation of Fe$_2$B consumed the surrounding Fe element in the [Fe–Ni] solid solution. Therefore, it can be inferred that the remaining Cr element spontaneously gathers around Fe$_2$B, which can be verified by the EDS results of Point D. Notably, Fig. 7 shows that the [Cr], [B], [Fe] elements are distributed at the edge phases with large lumps. Fig. 9(g) exhibits the subsequent formation of the (Cr, Fe)C phases.

3.3. Microstructure

The optical microstructures of the bottom, middle, and top of each specimen are shown in Fig. 10. Specimen 1# mainly contains columnar grains with direction and equiaxed grains without any direction. Large size columnar grains (length >200 μm), as shown in Fig. 10(a1), are found at the bottom of specimen 1# due to the larger temperature gradient (*G*) [48]. On the one hand, the formation of columnar grains results in the generation of solidified defects (cracks and pores) [27,49]. On the other hand, the directional grains weaken the isotropy of AM parts. This results in the reduction of the mechanical properties and fatigue life of remanufactured parts [50]. Therefore, these coarse columnar grains are generally considered to be unfavorable in AM parts. Furthermore, Fig. 10(a1) also shows that equiaxed grains are generated at the top of the first layer due to the poor directivity of heat dissipation. Fig. 10(a_2) demonstrates that the obvious interlayer boundary separates the coarse columnar grains at the bottom of the current layer from the equiaxed grains at the top of the previous layer. The growth direction of columnar grains is mainly perpendicular to the interlayer boundary, which is consistent with the direction of *G*. Fig. 10(a3) illustrates that the microstructure at the top of specimen 1# is mainly composed of equiaxed grains. Some small columnar grains are also observed because of the change of heat loss of the molten pool from the previous layer to air [51].

Fig. 10(b1–3) show that the microstructure of specimen 2# is different from that of specimen 1#. The interface between the remanufactured zone and the substrate of specimen 2# is cleaner than that of specimen 1# due to the precipitation of impurity elements in case of specimen 1# [16]. Fig. 10(b1) exhibits that the size of columnar grains decreases obviously due to the addition of Ti and B_4C. The thermal conductivity of the ceramic phases (such as TiC and TiB_2) is significantly lower than that of the metal alloy [52], which weakens the direction of heat conduction, thus resulting in the decrease of *G*. This phenomenon promoted the expected columnar to equiaxed transition in the composite coating. Phase and thermodynamic analysis show that the precipitation of each phase in specimen 2# was sequential. The continuously precipitated hard phases increased to the nucleation point during the solidification process. The growth of the final solidified matrix was restrained due to the previous precipitates. This behavior not only refined the microstructure, but also reduced the anisotropy of grains. Therefore, the microstructure of specimen 2# between layers is finer than that of specimen 1#. Fig. 10(b3) shows that the aspect ratio of grains at the top of specimen 2# is larger than that of specimen 1#, which is beneficial to improve the wear resistance according to the previous study [53].

3.4. Mechanical properties

3.4.1. Micro-hardness

The Vickers micro-hardness of each specimen was measured along the depth direction, and the corresponding results are shown in Fig. 11. The micro-hardness distribution occurs in the remanufactured zone, HAZ, and substrate zone. The average micro-hardness of specimen 1# with a typical AM 316 L microstructure is 232.33 HV, which is slightly higher than that of standard 45 steel (190.77 HV). The average micro-hardness of specimen 2# in the manufactured zone is 961.94 HV, which is 4.14 times that of specimen 1#, and 5.04 times that of standard 45 steel. Notably, the improvement of microhardness is mainly attributed to grain refinement strengthening and dispersion strengthening. On the one hand, stratification of the precipitates with different melting points leads to an increase in the nucleation sites and refining of the grains (see Fig. 10), which can improve the deformation resistance of the remanufactured zone. On the other hand, uniform distribution of TiC (3200 kg/mm^2) [54] and TiB_2 (3300 HV) [25] phases can hinder the movement of dislocations. In general, it is believed that lower hardness corresponds to better toughness, which is beneficial to improve the holding force of the matrix on the hard phases and reduce the generation and propagation of cracks [55]. Noteworthy, the micro-hardness in the

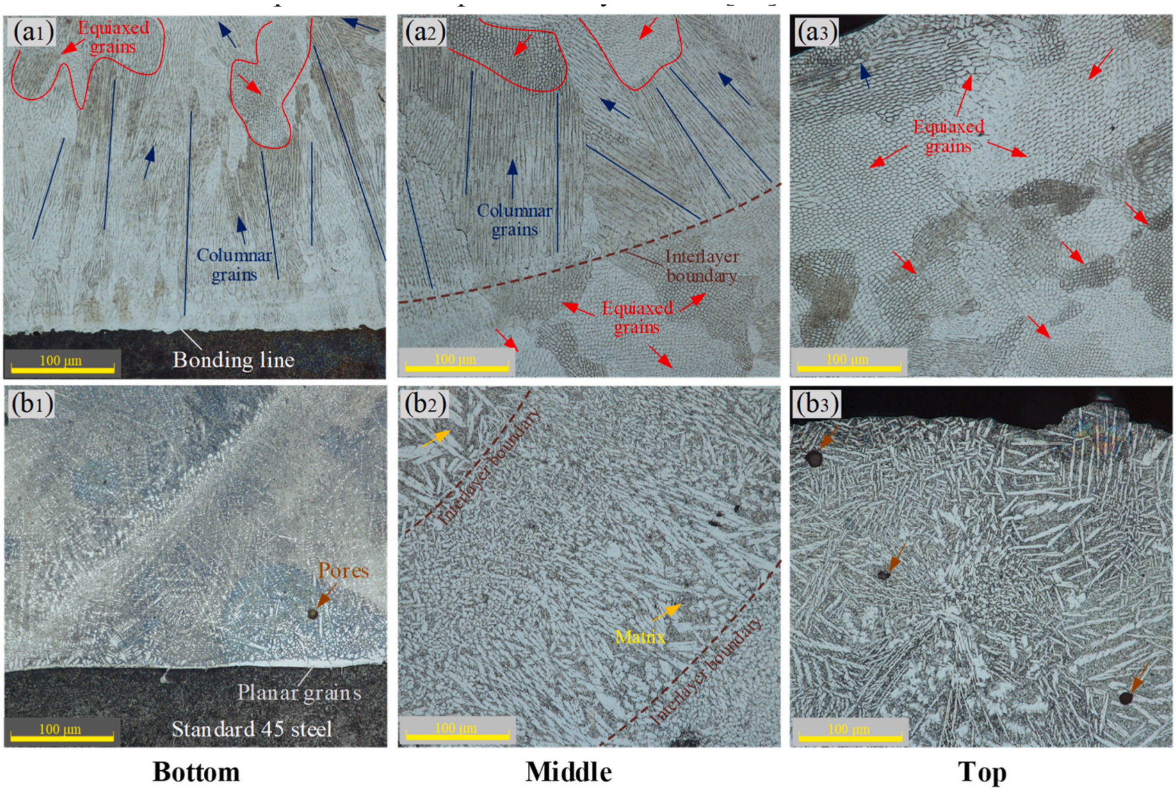

Fig. 10. The microstructure of remanufactured zone: (a) specimen 1#, and (b) specimen 2#.

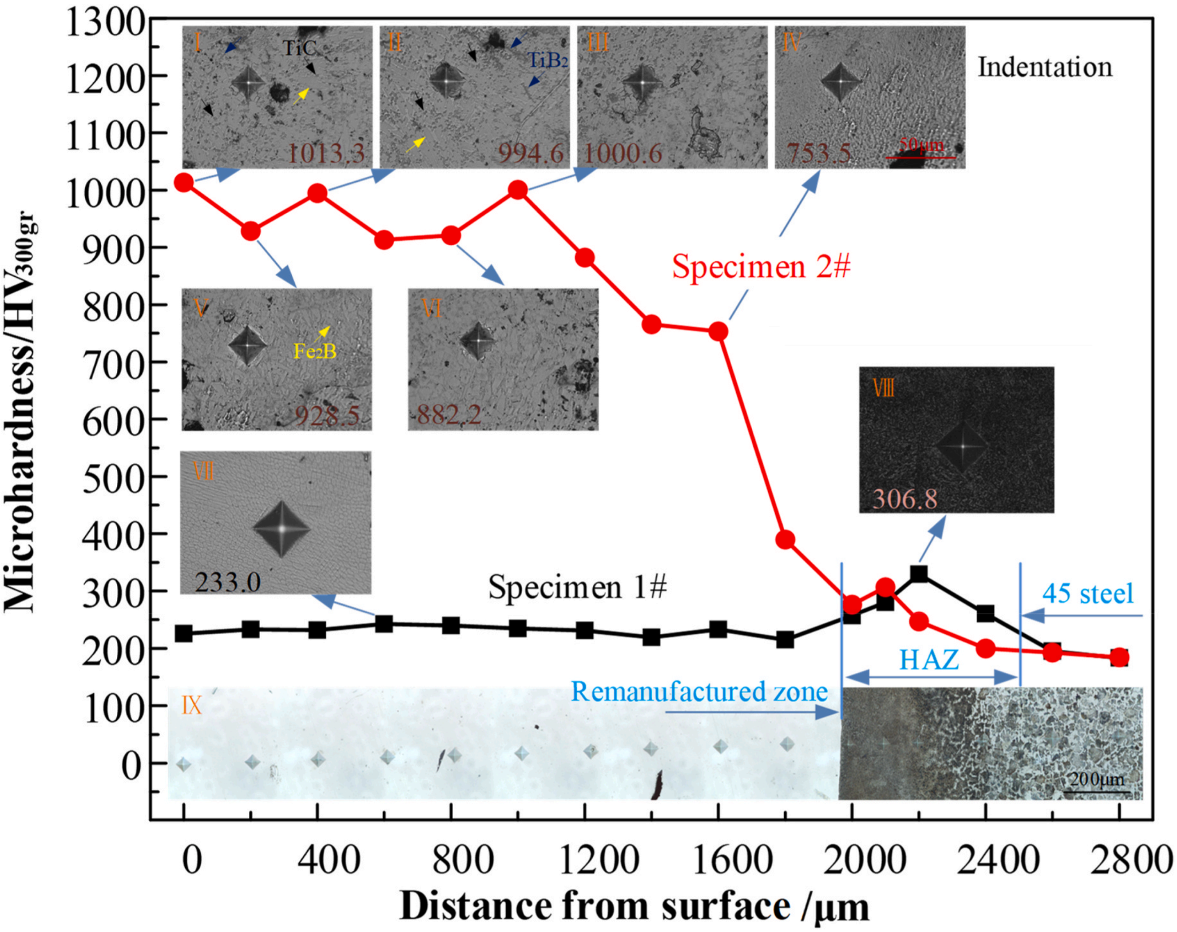

Fig. 11. The microhardness for specimen 1# and specimen 2#.

remanufactured zone of specimen 2# fluctuates slightly. The indentations I–III shown in Fig. 11 exhibit that numerous *in situ* formed hard phases are often found near high-hardness points; however, the microhardness at the indentations V and IV decreases slightly. Previous studies [48,56] reported that the solidification rate of liquid increases from top to bottom. The long solidification time at the top of the single-pass layer tends to form rich ceramic phases, as shown in Fig. 10 (b_2). Besides, the low density of the hard phases tends to make them float on the top of the molten pool under the Marangoni convection [26], thus the content of the reinforcement phases at the top of specimen 2# increases. Moreover, Fig. 11 also shows that the micro-hardness of HAZ is significantly higher than that of the substrate, which is attributed to the transformation of austenite to martensite during rapid cooling [57]. Furthermore, with the increase of the depth, the shape of martensite changes from acicular to flaky in the substrate, and its volume fraction also decreases, as shown in indentations VIII and IX. No sudden lapping in the micro-hardness at the bonding zone would provide sufficient bonding strength between the substrate and the remanufactured zone.

3.4.2. Wear performance

The wear performance is one of the important factors that aids in the evaluation of the service life of the remanufactured part, which can be revealed by the wear coefficient, wear loss, and worn surface morphology. Fig. 12 illustrates that the wear coefficient of different specimens fluctuates significantly in the initial stage of the experiment. The fluctuation of wear coefficient in specimen 2# with the wear time is the smallest, followed by specimen 1# and standard 45 steel. The volume loss (V_{loss}) is calculated by using the following Eq. (4):

$$\mathbf{V}_{loss} = \mathbf{A}_s \cdot L \tag{4}$$

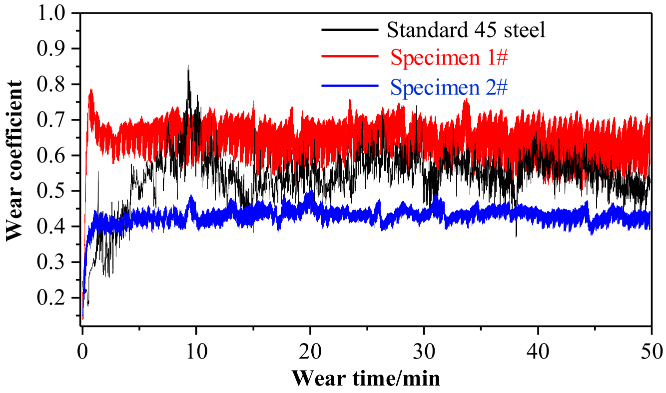

Fig. 12. Wear coefficient vs. time curves of different specimens.

where A_s represents the average area of 10 cross-sections (shown in Fig. 14) with an equal distance of 60 μm on the wear track and L denotes the reciprocating distance (6 mm). The average wear coefficient and volume loss are shown in Fig. 13. Noticeably, the volume loss of each specimen is consistent with its wear coefficient. The wear coefficient of specimen 2# shows the minimum value of 0.432, which is 0.78 and 0.67 times that of standard 45 steel and specimen 1#, respectively. The volume loss of specimen 2# exhibits the smallest value of 0.00785 cm^3, which is 7.8 and 2.8 less than that of specimen 1# and standard 45 steel, respectively.

In order to reveal the wear mechanism, the morphologies of the worn surface were obtained. Fig. 14 exhibits that significant plastic

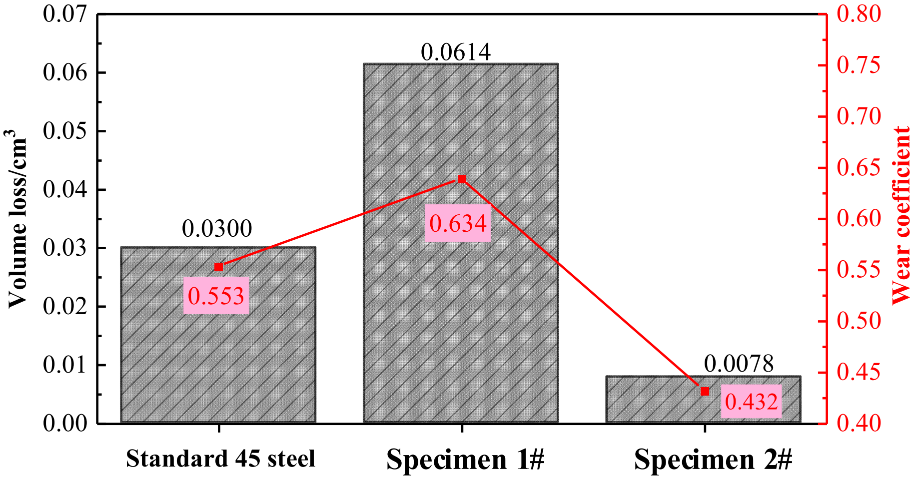

Fig. 13. The volume loss and wear coefficient of different specimens.

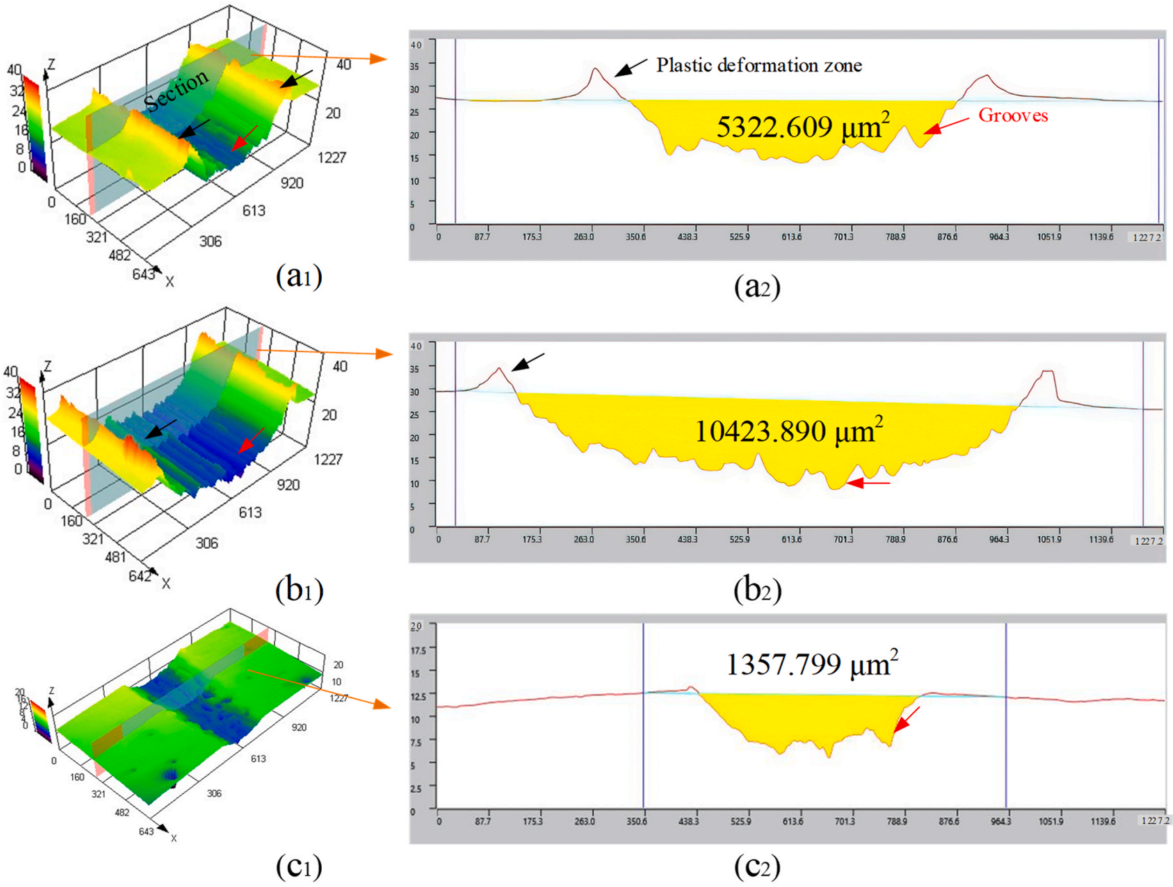

Fig. 14. 3D morphologies of wear tracks of (a) standard 45 steel, (b) specimen 1#, and (c) specimen 2#.

deformation occurs at the edge of the wear track and deep grooves are present in both specimen 1# and standard 45 steel. The friction pair with high hardness easily causes plastic deformation and micro-cutting of the softer matrix during the wear test. The wear debris with excellent toughness easily adheres to adhere to the surface of the friction pair, resulting in adhesive wear [58]. Furthermore, no obvious plastic deformation at the edge of the wear track is observed in specimen 2# as shown in Fig. 14(c1 and 2), and the width and depth of the wear track are significantly reduced compared to other specimens. These features are attributed to the high hardness and microstructural characteristics. The high hardness of specimen 2# preventes its plastic deformation and further results in a significant reduction in the wear rate. On the one hand, these exposed reinforcement phases can be used as the skeleton to carry the load of the friction pair and reduce the wear rate. On the other hand, the ceramic phases removed by micro-cutting play a lubricating role to some extent during the wear process, which not only reduces the wear coefficient but also improves the smoothness of the worn surface [59]. Therefore, based on the above analysis, it can be proved that the wear mechanism of specimen 2# is mainly abrasive wear.

Fig. 15 shows that the larger magnification optical images of

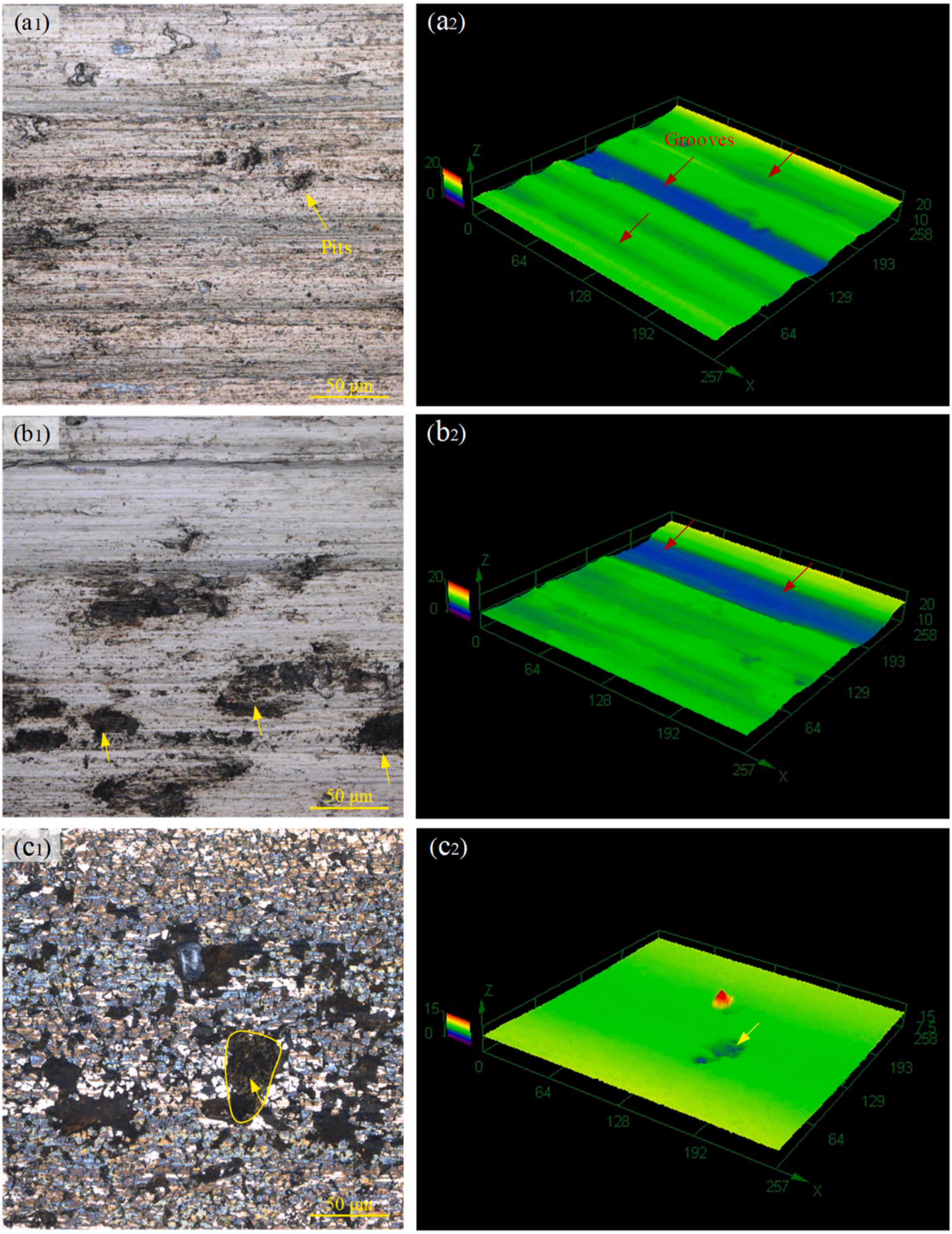

Fig. 15. Optical images of worn surfaces (a) standard 45 steel, (b) specimen 1#, and (c) specimen 2#.

different worn surfaces indicating that the number of pits on the worn surface of specimen 1# is more than that on the substrate. The parts fabricated by AM technology often acquire large residual stress [60]; moreover, the distribution of thermal stress is often regional. Therefore, these locally distributed residual stresses are more likely to cause the material to fall off from the worn surface under the repeated action of the friction pair, resulting in a large material loss of specimen 1#. Chen et al. [54] also observed a similar trend. Fig. 15(c) shows that the worn surface of specimen 2# is the smoothest. SEM images (Figs. 6 and 7) show that the *in situ* formed small primary phases of TiC, TiB_2, Cr_2C_3, and Fe_2B are embedded in the matrix and they cannot be easily peeled off under the action of reciprocating friction. The dispersion strengthening effect of these phases reduced the plastic deformation. Furthermore, a small amount of worn-out hard phases with high hardness played a lubricating role during the wear process, resulting in the smooth worn surface of specimen 2#. These dispersed hard phases reduced micro-cutting, thus specimen 2# showed excellent wear resistance.

4. Conclusions

In this study, surface remanufacturing of damaged standard 45 steel parts was successfully realized by *in situ* formed ceramic reinforced Fe-based coating fabricated via laser cladding. The surface morphology, phase composition, microstructure, and mechanical properties of the remanufactured specimens were analyzed and discussed in detail. The main conclusions of this study can be drawn as follows:

1. Addition of the active element Ti could consume the impurity elements in the molten pool, which not only improves the surface flatness but also cleans the interface between the remanufactured zone and the substrate.
2. The TiC, TiB_2, Cr_3C_2, and Fe_2B phases were *in situ* formed *in* remanufactured specimen 2#, which could continuously increase the nucleation sites and effectively refine the grains, and further promote the columnar to equiaxed transition during the solidification process.
3. The micro-hardness of specimen 2# is the highest with 961.94 $HV_{0.3}$, which is 4.14 times that of specimen 1# and 5.04 times that of standard 45 steel due to fine grain strengthening and dispersion strengthening.
4. The result of dry wear test shows that specimen 2# acquires the lowest friction coefficient of 0.432 and the smallest volume loss of 0.00785 cm^3 among all specimens. The wear mechanism changed from adhesive wear to abrasive wear due to the addition of Ti and B_4C.

Declaration of competing interest

No conflict of interest exists in the submission of this manuscript, and the manuscript is approved by all authors for publication. I would like to declare on behalf of my co-authors that the work described was original research that has not been published previously, and not under consideration for publication elsewhere, in whole or in part. The authors declare that they have no known competing financial interests or personal relationships that could have appeared to influence the work reported in this paper.

Acknowledgment

This work was support by the Fundamental Research Funds for the Central Universities (N2103004); the National Natural Science Foundation of China (52075088).

References

[1] E. Sundin, B. Bras, Making functional sales environmentally and economically beneficial through product remanufacturing, J. Clean. Prod. 13 (2005) 913–925, https://doi.org/10.1016/j.jclepro.2004.04.006.
[2] L. Sexton, S. Lavin, G. Byrne, A. Kennedy, Laser cladding of aerospace materials, J. Mater. Process. Technol. 122 (2002) 63–68, https://doi.org/10.1016/S0924-0136(01)01121-9.
[3] Z. Yan, W. Liu, Z. Tang, X. Liu, N. Zhang, M. Li, H. Zhang, Review on thermal analysis in laser-based additive manufacturing, Opt Laser. Technol. 106 (2018) 427–441, https://doi.org/10.1016/j.optlastec.2018.04.034.
[4] N. Shamsaei, A. Yadollahi, L. Bian, S.M. Thompson, An overview of Direct Laser Deposition for additive manufacturing; Part II: mechanical behavior, process parameter optimization and control, Addit. Manuf. 8 (2015) 12–35, https://doi.org/10.1016/j.addma.2015.07.002.
[5] Z. Sun, X. Tan, S.B. Tor, C.K. Chua, Simultaneously enhanced strength and ductility for 3D-printed stainless steel 316L by selective laser melting, NPG Asia Mater. 10 (2018) 127–136, https://doi.org/10.1038/s41427-018-0018-5.
[6] S. Zhou, Y. Zhao, X. Wang, W. Li, D. Chen, T.B. Sercombe, Enhanced corrosion resistance of Ti-5 wt.% TiN composite compared to commercial pure Ti produced by selective laser melting in HCl solution, J. Alloys Compd. 820 (2020) 153422, https://doi.org/10.1016/j.jallcom.2019.153422.
[7] B. Graf, A. Gumenyuk, M. Rethmeier, Laser metal deposition as repair technology for stainless steel and titanium alloys, Phys. Procedia 39 (2012) 376–381, https://doi.org/10.1016/j.phpro.2012.10.051.
[8] Y. Li, S. Dong, S. Yan, X. Liu, P. He, B. Xu, Surface remanufacturing of ductile cast iron by laser cladding Ni-Cu alloy coatings, Surf. Coating. Technol. 347 (2018) 20–28, https://doi.org/10.1016/j.surfcoat.2018.04.065.
[9] L. Zhu, S. Wang, H. Pan, C. Yuan, X. Chen, Research on remanufacturing strategy for 45 steel gear using H13 steel powder based on laser cladding technology, J. Manuf. Process. 49 (2020) 344–354, https://doi.org/10.1016/j.jmapro.2019.12.009.
[10] S. Da Sun, Q. Liu, M. Brandt, V. Luzin, R. Cottam, M. Janardhana, G. Clark, Effect of laser clad repair on the fatigue behaviour of ultra-high strength AISI 4340 steel, Mater. Sci. Eng. 606 (2014) 46–57, https://doi.org/10.1016/j.msea.2014.03.077.
[11] S. Saroj, C.K. Sahoo, M. Masanta, Microstructure and mechanical performance of TiC-Inconel825 composite coating deposited on AISI 304 steel by TIG cladding process, J. Mater. Process. Technol. 249 (2017) 490–501, https://doi.org/10.1016/j.jmatprotec.2017.06.042.
[12] R. Salloom, S.S. Joshi, N.B. Dahotre, S.G. Srinivasan, Laser surface engineering of B_4C/Fe nano composite coating on low carbon steel: experimental coupled with computational approach, Mater. Des. 190 (2020) 108576, https://doi.org/10.1016/j.matdes.2020.108576.
[13] P. Calloch, I.W.M. Brown, K.J.D. MacKenzie, J.V. Hanna, G.J. Rees, Synthesis and properties of new β-Sialon/TiN composites via a novel AlxTiy intermediate, Ceram. Int. 42 (2016) 2330–2338, https://doi.org/10.1016/j.ceramint.2015.10.029.
[14] M. Xie, C. Wu, S. Zhou, J. Jin, S. Zhao, D. Chen, TiB_2- and Fe_2P with nanotwins-reinforced Cu-based immiscible composites fabricated by selective laser melting: formation mechanism and wear behavior, J. Alloys Compd. 864 (2021) 158716, https://doi.org/10.1016/j.jallcom.2021.158716.
[15] Y. Zhao, T. Yu, J. Sun, S. Jiang, Microstructure and properties of laser cladded B_4C/TiC/Ni-based composite coating, Int. J. Refract. Metals Hard Mater. 86 (2020) 105112, https://doi.org/10.1016/j.ijrmhm.2019.105112.
[16] Ma Qunshuang, L. Yajiang, W. Juan, Effects of Ti addition on microstructure homogenization and wear resistance of wide-band laser clad Ni60/WC composite coatings, Int. J. Refract. Metals Hard Mater. 64 (2017) 225–233, https://doi.org/10.1016/j.ijrmhm.2016.11.002.
[17] J. Wang, L. Li, P. Lin, J. Wang, Effect of TiC particle size on the microstructure and tensile properties of TiCp/Ti6Al4V composites fabricated by laser melting deposition, Opt Laser. Technol. 105 (2018) 195–206, https://doi.org/10.1016/j.optlastec.2018.03.009.
[18] Y. Tan, H. Cai, X. Cheng, Z. Ma, Z. Xu, Z. Zhou, Microstructural and mechanical properties of in-situ micro-laminated TiC/Ti composite synthesised, Mater. Lett. 228 (2018) 1–4, https://doi.org/10.1016/j.matlet.2018.05.069.
[19] Y. bin Cao, S. xin Zhi, Q. Gao, X. tao Tian, T. Geng, X. Guan, C. Qin, Formation behavior of in-situ NbC in Fe-based laser cladding coatings, Mater. Char. 119 (2016) 159–165, https://doi.org/10.1016/j.matchar.2016.08.005.
[20] D. Tijo, M. Masanta, A.K. Das, In-situ TiC-TiB_2 coating on Ti-6Al-4V alloy by tungsten inert gas (TIG) cladding method: Part-I. Microstructure evolution, Surf. Coating. Technol. 344 (2018) 541–552, https://doi.org/10.1016/j.surfcoat.2018.03.082.
[21] X.H. Wang, S.L. Song, S.Y. Qu, Z.D. Zou, Characterization of in situ synthesized TiC particle reinforced Fe-based composite coatings produced by multi-pass overlapping GTAW melting process, Surf. Coating. Technol. 201 (2007) 5899–5905, https://doi.org/10.1016/j.surfcoat.2006.10.042.
[22] C. Cui, Z. Guo, H. Wang, J. Hu, In situ TiC particles reinforced grey cast iron composite fabricated by laser cladding of Ni-Ti-C system, J. Mater. Process. Technol. 183 (2007) 380–385, https://doi.org/10.1016/j.jmatprotec.2006.10.031.
[23] X.H. Wang, X.N. Pan, B.S. Du, S. Li, Production of in situ TiB2+TiC/Fe composite coating from precursor containing B_4C-TiO_2-Al powders by laser cladding, Trans. Nonferrous Met. Soc. China (English Ed. 23 (2013) 1689–1693, https://doi.org/10.1016/S1003-6326(13)62649-7.
[24] Y. Cai, Z. Luo, Y. Chen, S. Ao, Influence of CeO_2 on tribological behaviour of TiC/Fe-based composite coating, Surf. Eng. 33 (2017) 936–943, https://doi.org/10.1080/02670844.2017.1309742.
[25] J. Meng, X. Shi, S. Zhang, M. Wang, F. Xue, B. Liu, W. Cui, L. Bian, Friction and wear properties of TiN-TiB_2-Ni based composite coatings by argon arc cladding technology, Surf. Coating. Technol. 374 (2019) 437–447, https://doi.org/10.1016/j.surfcoat.2019.06.015.
[26] Y. Lin, Y. Lei, X. Li, X. Zhi, H. Fu, A study of TiB_2/TiB gradient coating by laser cladding on titanium alloy, Opt Laser. Eng. 82 (2016) 48–55, https://doi.org/10.1016/j.optlaseng.2016.01.016.
[27] Y. Zhao, T. Yu, J. Sun, L. Chen, Y. Chen, Effect of laser cladding on forming microhardness and tensile strength of YCF101 alloy powder in the different full lap joint modes, J. Alloys Compd. 820 (2020) 150230, https://doi.org/10.1016/j.jallcom.2019.04.046.
[28] T. Yu, J. Sun, W. Qu, Y. Zhao, L. Yang, Influences of z-axis increment and analyses of defects of AISI 316L stainless steel hollow thin-walled cylinder, Int. J. Adv. Manuf. Technol. 97 (2018) 2203–2220, https://doi.org/10.1007/s00170-018-2083-x.
[29] L. Wang, S.D. Felicelli, P. Pratt, Residual stresses in LENS-deposited AISI 410 stainless steel plates, Mater. Sci. Eng. 496 (2008) 234–241, https://doi.org/10.1016/j.msea.2008.05.044.
[30] R.J. Moat, A.J. Pinkerton, L. Li, P.J. Withers, M. Preuss, Residual stresses in laser direct metal deposited Waspaloy, Mater. Sci. Eng. 528 (2011) 2288–2298, https://doi.org/10.1016/j.msea.2010.12.010.

[31] N. Hutasoit, V. Luzin, A. Blicblau, W. Yan, M. Brandt, R. Cottam, Fatigue life of laser clad hardfacing alloys on AISI 4130 steel under rotary bending fatigue test, Int. J. Fatig. 72 (2015) 42–52, https://doi.org/10.1016/j.ijfatigue.2014.11.001.

[32] L. Chen, Y. Zhao, B. Song, T. Yu, Z. Liu, Modeling and simulation of 3D geometry prediction and dynamic solidification behavior of Fe-based coatings by laser cladding, Opt Laser. Technol. 139 (107009) (2021), https://doi.org/10.1016/j.optlastec.2021.107009.

[33] H. Zeinali Moghaddam, M. Sharifitabar, G. Roudini, Microstructure and wear properties of Fe–TiC composite coatings produced by submerged arc cladding process using ferroalloy powder mixtures, Surf. Coating. Technol. 361 (2019) 91–101, https://doi.org/10.1016/j.surfcoat.2019.01.053.

[34] Y. Sun, L. Jin, Y. Gong, X. Wen, G. Yin, Q. Wen, B. Tang, Experimental evaluation of surface generation and force time-varying characteristics of curvilinear grooved micro end mills fabricated by EDM, J. Manuf. Process. 73 (2022) 799–814, https://doi.org/10.1016/j.jmapro.2021.11.049.

[35] Y. Li, X. Huang, I. Horváth, G. Zhang, GMAW-based additive manufacturing of inclined multi-layer multi-bead parts with flat-position deposition, J. Mater. Process. Technol. 262 (2018) 359–371, https://doi.org/10.1016/j.jmatprotec.2018.07.010.

[36] G. Bi, B. Schürmann, A. Gasser, K. Wissenbach, R. Poprawe, Development and qualification of a novel laser-cladding head with integrated sensors, Int. J. Mach. Tool Manufact. 47 (2007) 555–561.

[37] T. DebRoy, H.L. Wei, J.S. Zuback, T. Mukherjee, J.W. Elmer, J.O. Milewski, A. M. Beese, A. Wilson-Heid, A. De, W. Zhang, Additive manufacturing of metallic components – process, structure and properties, Prog. Mater. Sci. 92 (2018) 112–224, https://doi.org/10.1016/j.pmatsci.2017.10.001.

[38] L. Peng, J. Shengqin, Z. Xiaoyan, H. Qianwu, X. Weihao, Direct laser fabrication of thin-walled metal parts under open-loop control, Int. J. Mach. Tool Manufact. 47 (2007) 996–1002, https://doi.org/10.1016/j.ijmachtools.2006.06.017.

[39] H. Tan, W. Shang, F. Zhang, A.T. Clare, X. Lin, J. Chen, W. Huang, Process mechanisms based on powder flow spatial distribution in direct metal deposition, J. Mater. Process. Technol. 254 (2018) 361–372, https://doi.org/10.1016/j.jmatprotec.2017.11.026.

[40] K. Zhang, S. Wang, W. Liu, X. Shang, Characterization of stainless steel parts by laser metal deposition shaping, Mater. Des. 55 (2014) 104–119, https://doi.org/10.1016/j.matdes.2013.09.006.

[41] M. Zhang, G.L. Zhao, X.H. Wang, S.S. Liu, W.L. Ying, Microstructure evolution and properties of in-situ ceramic particles reinforced Fe-based composite coating produced by ultrasonic vibration assisted laser cladding processing, Surf. Coating. Technol. 403 (2020) 126445, https://doi.org/10.1016/j.surfcoat.2020.126445.

[42] J. Tang, Mechanical and tribological properties of the TiC-TiB_2 composite coating deposited on 40Cr-steel by electro spark deposition, Appl. Surf. Sci. 365 (2016) 202–208, https://doi.org/10.1016/j.apsusc.2015.12.198.

[43] Q. Wu, W. Li, N. Zhong, W. Gang, W. Haishan, Microstructure and wear behavior of laser cladding VC-Cr_7C_3 ceramic coating on steel substrate, Mater. Des. 49 (2013) 10–18, https://doi.org/10.1016/j.matdes.2013.01.067.

[44] L. Chen, T. Yu, P. Xu, B. Zhang, In-situ NbC reinforced Fe-based coating by laser cladding: simulation and experiment, Surf. Coating. Technol. 412 (2021) 127027, https://doi.org/10.1016/j.surfcoat.2021.127027.

[45] X. He, X. Zhang, Y. Li, J. Huang, Effect of Mo on microstructure and mechanical properties of Nb-Ti-C-B multiphase alloy, J. Alloys Compd. 551 (2013) 578–583, https://doi.org/10.1016/j.jallcom.2012.11.052.

[46] J.H. Ye, D.L. Hu, Utility Inorganic Materials Thermodynamics Data Handbook, second ed., Metallurgy Industry Press, Beijing, 2002.

[47] H. Chen, Y. Lu, Y. Sun, Y. Wei, X. Wang, D. Liu, Coarse TiC particles reinforced H13 steel matrix composites produced by laser cladding, Surf. Coating. Technol. 395 (2020) 125867, https://doi.org/10.1016/j.surfcoat.2020.125867.

[48] Z. Liu, H. Qi, Effects of substrate crystallographic orientations on crystal growth and microstructure formation in laser powder deposition of nickel-based superalloy, Acta Mater. 87 (2015) 248–258, https://doi.org/10.1016/j.actamat.2014.12.046.

[49] Y. Zhao, J. Sun, J. Li, Effect of rare earth oxide on the properties of laser cladding layer and machining vibration suppressing in side milling, Appl. Surf. Sci. 321 (2014) 387–395, https://doi.org/10.1016/j.apsusc.2014.09.195.

[50] M.J. Bermingham, D.H. StJohn, J. Krynen, S. Tedman-Jones, M.S. Dargusch, Promoting the columnar to equiaxed transition and grain refinement of titanium alloys during additive manufacturing, Acta Mater. 168 (2019) 261–274, https://doi.org/10.1016/j.actamat.2019.02.020.

[51] J. Sun, Y. Zhao, L. Yang, X. Zhao, W. Qu, T. Yu, Effect of shielding gas flow rate on cladding quality of direct laser fabrication AISI 316L stainless steel, J. Manuf. Process. 48 (2019) 51–65, https://doi.org/10.1016/j.jmapro.2019.10.011.

[52] P. Farahmand, S. Liu, Z. Zhang, R. Kovacevic, Laser cladding assisted by induction heating of Ni–WC composite enhanced by nano-WC and La_2O_3, Ceram. Int. 40 (2014) 15421–15438, https://doi.org/10.1016/j.ceramint.2014.06.097.

[53] Y. Lin, C. Jiang, Z. Lin, Q. Chen, Y. Lei, H. Fu, Laser in-situ synthesis of high aspect ratio TiB fiber bundle reinforced titanium matrix composite coating, Opt Laser. Technol. 115 (2019) 364–373, https://doi.org/10.1016/j.optlastec.2019.02.047.

[54] L. Song, G. Zeng, H. Xiao, X. Xiao, S. Li, Repair of 304 stainless steel by laser cladding with 316L stainless steel powders followed by laser surface alloying with WC powders, J. Manuf. Process. 24 (2016) 116–124, https://doi.org/10.1016/j.jmapro.2016.08.004.

[55] L. Chen, Y. Zhao, X. Chen, T. Yu, P. Xu, Repair of spline shaft by laser-cladding coarse TiC reinforced Ni-basedcoating: Process, microstructure and properties, Ceram. Int. 47 (2021) 30113–30128, https://doi.org/10.1016/j.ceramint.2021.07.189.

[56] Y. Zhao, Y. Koizumi, K. Aoyagi, D. Wei, K. Yamanaka, A. Chiba, Molten pool behavior and effect of fluid flow on solidification conditions in selective electron beam melting (SEBM) of a biomedical Co-Cr-Mo alloy, Addit. Manuf. 26 (2019) 202–214, https://doi.org/10.1016/j.addma.2018.12.002.

[57] S. Liu, K.M. Hong, C. Katinas, Y.C. Shin, Multiphysics modeling of phase transformation and microhardness evolution in laser direct deposited Ti6Al4V, J. Manuf. Process. 45 (2019) 579–587, https://doi.org/10.1016/j.jmapro.2019.07.027.

[58] L. Yang, T. Yu, M. Li, Y. Zhao, J. Sun, Microstructure and wear resistance of in-situ synthesized Ti(C, N) ceramic reinforced Fe-based coating by laser cladding, Ceram. Int. 44 (2018) 22538–22548, https://doi.org/10.1016/j.ceramint.2018.09.025.

[59] Z. Ma, Q Wang, H. Chen, L. Chen, S. Qu, Z. Wang, T. Yu, A grinding force predictive model and experimental validation for thelaser-assisted grinding (LAG) process of zirconia ceramic, J. Mater. Process. Tech. 302 (117492) (2022), https://doi.org/10.1016/j.jmatprotec.2022.117492.

[60] F. Liu, X. Lin, G. Yang, M. Song, J. Chen, W. Huang, Microstructure and residual stress of laser rapid formed Inconel 718 nickel-base superalloy, Opt Laser. Technol. 43 (2011) 208–213, https://doi.org/10.1016/j.optlastec.2010.06.015.